International Journal of Thermal Sciences 48 (2009) 948–963

Contents lists available at ScienceDirect

International Journal of Thermal Sciences

www.elsevier.com/locate/ijts

Turbulent mixed convection in a shallow enclosure with a series of heat generating components

Mayur T. Bhoite, G.S.V.L. Narasimham *

Department of Mechanical Engineering, Indian Institute of Science, Bangalore, Bangalore 560 012, India

ARTICLE INFO

Article history:
Received 4 March 2007
Received in revised form 23 June 2008
Accepted 27 August 2008
Available online 23 September 2008

Keywords:
Turbulent mixed convection
Enclosure
Volumetric heat generation
Pressure drop

ABSTRACT

Turbulent mixed convection flow and heat transfer in a shallow enclosure with and without partitions and with a series of block-like heat generating components is studied numerically for a range of Reynolds and Grashof numbers with a time-dependent formulation. The flow and temperature distributions are taken to be two-dimensional. Regions with the same velocity and temperature distributions can be identified assuming repeated placement of the blocks and fluid entry and exit openings at regular distances, neglecting the end wall effects. One half of such module is chosen as the computational domain taking into account the symmetry about the vertical centreline. The mixed convection inlet velocity is treated as the sum of forced and natural convection components, with the individual components delineated based on pressure drop across the enclosure. The Reynolds number is based on forced convection velocity. Turbulence computations are performed using the standard k–ϵ model and the Launder–Sharma low-Reynolds number k–ϵ model. The results show that higher Reynolds numbers tend to create a recirculation region of increasing strength in the core region and that the effect of buoyancy becomes insignificant beyond a Reynolds number of typically 5×10^5. The Euler number in turbulent flows is higher by about 30 per cent than that in the laminar regime. The dimensionless inlet velocity in pure natural convection varies as $Gr^{1/3}$. Results are also presented for a number of quantities of interest such as the flow and temperature distributions, Nusselt number, pressure drop and the maximum dimensionless temperature in the block, along with correlations.

1. Introduction

In general, in any forced convection heat transfer situation, buoyancy effects are always present and interact with the forced flow effects. If the buoyancy effect is smaller, forced convection tends to predominate and if the buoyancy is larger, the heat transfer is dominated by natural convection. When there is a significant interaction between forced and free convection effects, the heat transfer mechanism is called combined free-forced or mixed convection. In this case both the Reynolds and the Grashof numbers become important parameters. Mixed convection in enclosures is currently receiving increasing attention in the literature.

In a previous paper [1], the results of a numerical study on the laminar mixed convection in a shallow enclosure with a series of block-like heat generating components are reported for a range of Reynolds and Grashof numbers along with a summary of the important previous work done mostly in the area of laminar mixed convection in enclosures. In the literature review presented here, attention is focused mostly on the work carried out in the area of turbulent forced or mixed enclosure convection which has relevance to various applications like ventilation and air-conditioning, contaminant removal, cold stores and electronics cooling.

The review article by Linden [2] presents a summary of various important investigations in the area of natural ventilation of buildings. The flow pattern was shown to be governed by the exchange between the interior space and the external ambient.

Nielsen et al. [3] investigated the interaction of buoyancy created due to human occupancy with forced air circulation in air-conditioned rooms with a uniform heat flux boundary condition on the floor. Primitive variable calculations with steady state equations and with a high-Reynolds number k–ϵ model of turbulence are performed. It was found that higher values of Archimedes number create undesirable draft in occupied zone. Nielsen [4] determined the distribution of contaminants like welding smoke in a two-dimensional ventilated enclosure with a side inlet at the top of a vertical wall and a side outlet at the bottom of the opposing vertical wall. The variation of the jet penetration length with Archimedes number presented in this study serves as a guideline for air-conditioning designers.

Lage and Bejan [5] performed a numerical analysis of turbulent mass transport in a slot ventilated cavity with a low Reynolds number k–ϵ turbulence model and presented correlations for the

* Corresponding author. Tel.: +91 80 22932971; fax: +91 80 23600648.
E-mail address: mecgsvln@mecheng.iisc.ernet.in (G.S.V.L. Narasimham).

1290-0729/$ – see front matter
doi:10.1016/j.ijthermalsci.2008.08.010

Nomenclature

a	thermal diffusivity of the fluid	$m^{-2}\,s^{-1}$
Ar	Archimedes number, $= Gr/Re^2$	
c_p	constant pressure specific heat capacity of the fluid	$J\,kg^{-1}\,K^{-1}$
c_s	specific heat capacity of the solid	$J\,kg^{-1}\,K^{-1}$
$c_\mu, c_{\epsilon1}, c_{\epsilon2}, c_{\epsilon3}$	various constants in Eq. (7)	
D_k	destruction of turbulent kinetic energy	$m^2\,s^{-3}$
E	destruction of turbulent dissipation rate	$m^2\,s^{-4}$
Eu	Euler number, $= \Delta p^*/Re^2$	
f_μ, f_1, f_2	various constants in Eq. (7)	
g	gravitational acceleration	$m\,s^{-2}$
G_k	turbulent production by buoyancy	$m^2\,s^{-3}$
Gr	Grashof number, $= g\beta\Delta T H^3/\nu^2$	
H	height of the enclosure	m
H_1	height of the heat generating block	m
k	turbulent kinetic energy	$m^2\,s^{-2}$
L_i $(i = 1–4)$	various dimensions	m
Nu	Nusselt number	
p	excess pressure over the hydrostatic	Pa
P_k	turbulent shear production	$m^2\,s^{-3}$
Pr	Prandtl number, $= \nu/a$	
$\dot{Q}_v$	volumetric heat generation rate in the solid	$W\,m^{-3}$
r_p, r_T	parameters for comparison	
Ra	Rayleigh number, $= Gr\,Pr$	
Re	Reynolds number, $= v_{in,fc}H/\nu$	
S_ϵ	yap correction source term	$m^2\,s^{-4}$
t	time	s
T	temperature	K
u, v	velocity components in the x and y directions	$m\,s^{-1}$
u_*	friction velocity scale	$m\,s^{-1}$
x, y	Cartesian coordinates	m

Greek symbols

α	heat transfer coefficient	$W\,m^{-2}\,K^{-1}$
β	volumetric expansion coefficient of the fluid	K^{-1}
Δ	length scale in Yoshizawa model	m
Δ_w^+	friction coordinate of the first mesh spacing	
Δp	pressure drop across the enclosure	Pa
ΔT	characteristic temperature difference, $= \dot{Q}_v H^2/\lambda$	K
$\Delta x, \Delta y$	grid metrics of a computational cell	m
ϵ	turbulent kinetic energy dissipation rate	$m^2\,s^{-3}$
κ	von Karman constant	
λ	thermal conductivity of the fluid	$W\,m^{-1}\,K^{-1}$
λ_s	thermal conductivity of the solid	$W\,m^{-1}\,K^{-1}$
ν	kinematic viscosity of the fluid	$m^2\,s^{-1}$
ρ	density of the fluid	$kg\,m^{-3}$
ρ_s	density of the solid	$kg\,m^{-3}$
$\sigma_T, \sigma_k, \sigma_\epsilon$	turbulent Prandtl numbers for T, k and ϵ	
ψ	stream function	$m^2\,s^{-1}$

Subscripts

fc	forced convection
in	inlet
max	maximum
nc	natural convection contribution in mixed convection
pnc	pure natural convection
t	turbulent quantity
turb	turbulizing limit
w	wall

Superscript

$*$	dimensionless quantity
$+$	wall-friction scaled quantity

ventilation efficiency. The investigation was extended in [6] to the study of mass transport from the cavity with discrete volumetric mass generation. The results include the effect of source location, inlet and outlet locations and Reynolds number on the contaminant removal. The optimal inlet–outlet configurations for various source locations were reported.

Murakami et al. [7] reported three-dimensional turbulent flow and contaminant concentration computations and measurements for ventilated rooms. Following good agreement between computations and measurements, the authors regard numerical prediction of room air distribution to be a very promising technique. Kurabuchi and Kusuda [8] predicted the air flow patterns in a room with two windows on a vertical wall, a door in the opposing wall and an interior draft chamber using a large-eddy simulation model. The results were found to be in excellent agreement with their measured values.

Representative studies focusing attention on the modeling of turbulent mixed convection in cold storage rooms are Wang and Touber [9], van Gerwen and van Oort [10,11] and Hoang et al. [12].

Computations of two-dimensional turbulent mixed convective flow inside an enclosure with inlet and outlet openings situated at the top of the left and right vertical walls and a left-wall-mounted isoflux heat source were carried out by Papanicolaou and Jaluria [13] for application to electronics cooling. The production of turbulence at that location was predominantly due to shear. A small amount of turbulence was generated due to buoyancy in the thermal boundary layer of the heat source.

The objective of the present work is to extend the laminar enclosure mixed convection study reported earlier [1] to analyze the effects of turbulence on the quantities of engineering interest like maximum dimensionless temperature and pressure drop for turbulent regime. The geometry is a shallow enclosure with a series of floor-mounted block-like heat generating components and with multiple floor admission and ceiling extraction openings. The enclosure can be visualized as an electronic cabinet with electronic packages or an air-conditioned computer room.

Turbulent natural convection computations of Henkes [14] and Henkes et al. [15] for a differentially heated square cavity with different k–ϵ models reveal that the performance of the standard k–ϵ model [16] is characterized by a rapid increase in the turbulent viscosity and heat transfer rate above a certain Rayleigh number and that the Jones–Launder model [17] yields better heat transfer predictions compared to other low-Reynolds number models, despite the delayed transition. Papanicolaou and Belessiotis [18] compare the performance of three low-Reynolds number models and report that the Launder–Sharma model [19,20], which is the Jones–Launder model with modified coefficients, is able to predict the transition at the right location on the isoflux wall of a cylindrical enclosure, in which transient natural convection is taking place at a high Rayleigh number. Hanjalic and Vasic [21] reported turbulent heat transfer computations with Launder–Sharma model for differentially heated enclosures, enclosures with different wall thermal boundary conditions and for partially-divided enclosures.

Based on the aforementioned discussion, the standard k–ϵ model [14,15] and the Launder–Sharma low-Reynolds number k–ϵ model [19,20] (referred to as Model 1 and Model 2, respectively) are employed in the present study. For a proper prediction of near-wall length scales in recirculating regions, the Yap correction sug-

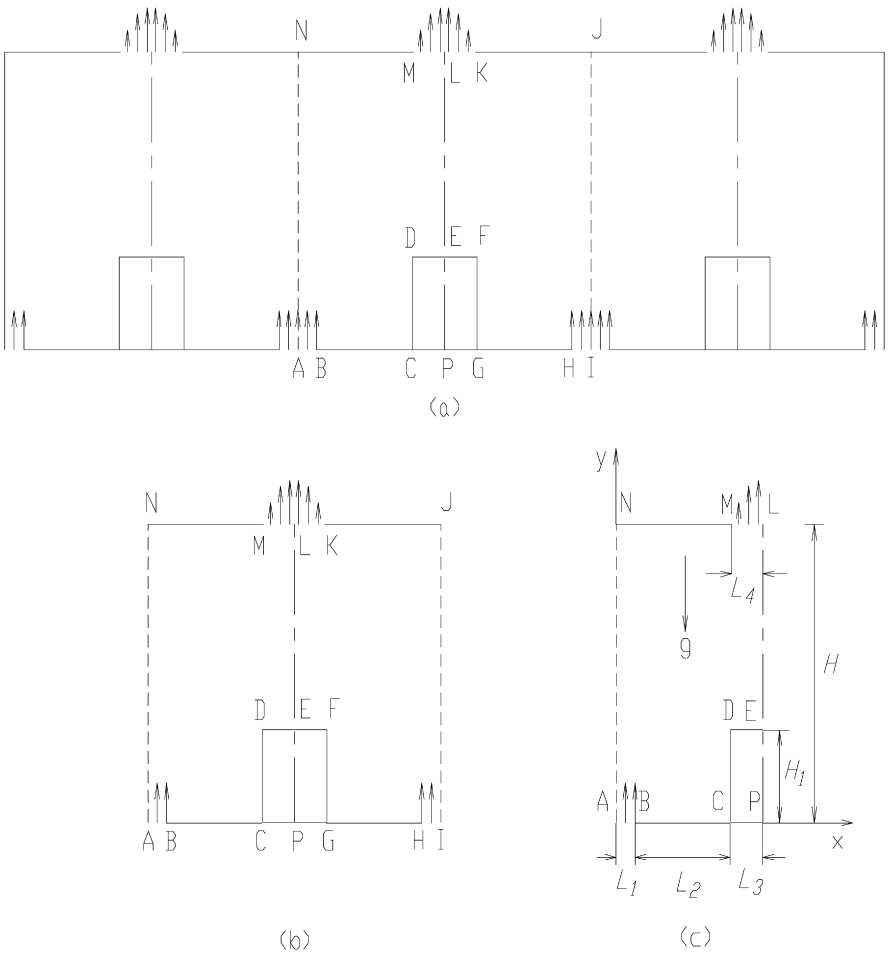

Fig. 1. Physical model and coordinate system.

gested in Ince and Launder [22] is included in the turbulent kinetic energy dissipation rate equation of Launder–Sharma model.

2. Physical model and coordinate system

The physical model, shown in Fig. 1(a), is a shallow enclosure with repeated placement of floor mounted heat generating components and floor admission and ceiling extraction openings. The components and openings are deployed in such a way that, neglecting end wall effects, they form a series of modules in which flow and temperature fields are identical. One such module with a heat generating component CDEFG (assumed to be a solid block), floor admission openings of half width (AB, HI) on either side of the floor and a ceiling extraction opening (KLM) is chosen for analysis and this module is shown in Fig. 1(b). The symmetry boundaries AN and IJ are either free boundaries (Problem 1) or solid boundaries (Problem 2). The symmetry of the velocity and temperature fields about the mid vertical plane LEP further facilitates the choice of one half of the module domain ABCPELMNA for the analysis. The computational domain is shown in Fig. 1(c), in which the origin is placed at the bottom left corner with positive direction of the x-axis directed towards right and the positive direction of the y-axis directed vertically upwards. The gravity vector is oriented parallel to the y-axis with an opposite sense.

3. Mathematical formulation

The flow and temperature distributions are governed by the time averaged continuity, Navier–Stokes, fluid and solid energy and turbulence closure equations. The radiative heat transfer, viscous heat dissipation and compressibility effects are considered to be negligible. The working medium is air. The effect of the density variation causing the buoyancy force is taken into account through the Oberbeck–Boussinésq approximation. Other thermophysical properties of the fluid and the thermophysical properties of the solid are assumed to be independent of temperature.

3.1. Governing equations

The governing equations in dimensionless form read:

Continuity equation:

$$\frac{\partial u^*}{\partial x^*} + \frac{\partial v^*}{\partial y^*} = 0 \tag{1}$$

Momentum equation in x^*-direction:

$$\frac{\partial u^*}{\partial t^*} + \frac{\partial}{\partial x^*}(u^{*2}) + \frac{\partial}{\partial y^*}(v^* u^*) = -\frac{\partial p^*}{\partial x^*} + \frac{\partial}{\partial x^*}\left[2\left(1+\nu_t^*\right)\frac{\partial u^*}{\partial x^*}\right] + \frac{\partial}{\partial y^*}\left[\left(1+\nu_t^*\right)\left(\frac{\partial u^*}{\partial y^*} + \frac{\partial v^*}{\partial x^*}\right)\right] \tag{2}$$

Momentum equation in y^*-direction:

$$\frac{\partial v^*}{\partial t^*} + \frac{\partial}{\partial x^*}(u^* v^*) + \frac{\partial}{\partial y^*}(v^{*2})$$

$$= -\frac{\partial p^*}{\partial y^*} + \frac{\partial}{\partial y^*}\left[2\left(1+\nu_t^*\right)\frac{\partial v^*}{\partial y^*}\right] + \frac{\partial}{\partial x^*}\left[\left(1+\nu_t^*\right)\left(\frac{\partial u^*}{\partial y^*}+\frac{\partial v^*}{\partial x^*}\right)\right] + Gr\,T^* \tag{3}$$

Energy equation in the fluid:

$$\frac{\partial T^*}{\partial t^*} + \frac{\partial}{\partial x^*}(u^*T^*) + \frac{\partial}{\partial y^*}(v^*T^*) = \frac{\partial}{\partial x^*}\left[\left(\frac{1}{Pr}+\frac{\nu_t^*}{\sigma_T}\right)\frac{\partial T^*}{\partial x^*}\right] + \frac{\partial}{\partial y^*}\left[\left(\frac{1}{Pr}+\frac{\nu_t^*}{\sigma_T}\right)\frac{\partial T^*}{\partial y^*}\right] \tag{4}$$

Energy equation in the solid:

$$\rho_s^* c_s^* \frac{\partial T_s^*}{\partial t^*} = \frac{\lambda_s^*}{Pr}\left(\frac{\partial^2 T_s^*}{\partial x^{*2}} + \frac{\partial^2 T_s^*}{\partial y^{*2}}\right) + \frac{1}{Pr} \tag{5}$$

Turbulent kinetic energy equation:

$$\frac{\partial k^*}{\partial t^*} + \frac{\partial}{\partial x^*}(u^*k^*) + \frac{\partial}{\partial y^*}(v^*k^*) = \frac{\partial}{\partial x^*}\left[\left(1+\frac{\nu_t^*}{\sigma_k}\right)\frac{\partial k^*}{\partial x^*}\right] + \frac{\partial}{\partial y^*}\left[\left(1+\frac{\nu_t^*}{\sigma_k}\right)\frac{\partial k^*}{\partial y^*}\right] + P_k^* + G_k^* - \epsilon^* + D_k^* \tag{6}$$

Turbulent kinetic energy dissipation rate equation:

$$\frac{\partial \epsilon^*}{\partial t^*} + \frac{\partial}{\partial x^*}(u^*\epsilon^*) + \frac{\partial}{\partial y^*}(v^*\epsilon^*) = \frac{\partial}{\partial x^*}\left[\left(1+\frac{\nu_t^*}{\sigma_\epsilon}\right)\frac{\partial \epsilon^*}{\partial x^*}\right] + \frac{\partial}{\partial y^*}\left[\left(1+\frac{\nu_t^*}{\sigma_\epsilon}\right)\frac{\partial \epsilon^*}{\partial y^*}\right] + \left[c_{\epsilon 1} f_1\left(P_k^* + c_{\epsilon 3} G_k^*\right) - c_{\epsilon 2} f_2 \epsilon^*\right]\frac{\epsilon^*}{k^*} + E^* \tag{7}$$

where

$$P_k^* = \nu_t^*\left[2\left(\frac{\partial u^*}{\partial x^*}\right)^2 + 2\left(\frac{\partial v^*}{\partial y^*}\right)^2 + \left(\frac{\partial u^*}{\partial y^*}+\frac{\partial v^*}{\partial x^*}\right)^2\right] \tag{8}$$

and

$$G_k^* = -\nu_t^*\frac{Gr}{\sigma_T}\left(\frac{\partial T^*}{\partial y^*}\right) \tag{9}$$

The terms P_k^* and G_k^* express the rate of production of turbulence by shear and buoyancy respectively. The other terms depend upon the model and are as follows:

- Standard k–ϵ model (Model 1) [14,15]: $\nu_t^* = (c_\mu k^{*2})/\epsilon^*$, $c_\mu = 0.09$, $c_{\epsilon 1} = 1.44$, $c_{\epsilon 2} = 1.92$, $\sigma_T = 0.9$, $\sigma_k = 1.0$, $\sigma_\epsilon = 1.3$, $f_\mu = f_1 = f_2 = 1.0$, $D_k^* = E^* = 0$.
- Launder–Sharma low Reynolds number k–ϵ model (Model 2) [19,20]: $\nu_t^* = (c_\mu f_\mu k^{*2})/\epsilon^*$, $c_\mu = 0.09$, $c_{\epsilon 1} = 1.44$, $c_{\epsilon 2} = 1.92$, $\sigma_T = 0.9$, $\sigma_k = 1.0$, $\sigma_\epsilon = 1.3$, $f_\mu = \exp[-2.5/(1 + Re_t/50)]$, $f_1 = 1$, $f_2 = 1.0 - \exp(-Re_t^2)$ where $Re_t = k^{*2}/\epsilon^*$.

$$D_k^* = -2\left[\left(\frac{\partial\sqrt{k^*}}{\partial x^*}\right)^2 + \left(\frac{\partial\sqrt{k^*}}{\partial y^*}\right)^2\right] \tag{10}$$

$$E^* = -2\nu_t^*\left[\left(\frac{\partial^2 u^*}{\partial y^{*2}}\right)^2 + \left(\frac{\partial^2 v^*}{\partial x^{*2}}\right)^2\right] \tag{11}$$

Additionally, following [22], the Yap source term S_ϵ^* to be included in the turbulent kinetic energy dissipation rate equation is as follows:

$$S_\epsilon^* = 0.83\left(\frac{k^{*1.5}}{\tilde{\epsilon^*} c \Delta_w^*} - 1\right)\left(\frac{k^{*1.5}}{\tilde{\epsilon^*} c \Delta_w^*}\right)^2 \frac{\epsilon^*}{k^*}$$

$$\tilde{\epsilon^*} = \epsilon^* - D_k^* \tag{12}$$

where $c = 2.5$ and Δ_w^* is dimensionless distance from the wall. Compared to the original reference [22], the symbols $\tilde{\epsilon^*}$ and ϵ^* are interchanged here to represent the dimensionless turbulent kinetic energy dissipation rate in both the models by a common notation ϵ^*.

Apart from *Gr*, *Pr* and *Re* defined in the nomenclature, the definitions of the dimensionless quantities appearing in the above equations are as follows:

$$x^* = \frac{x}{H}, \quad y^* = \frac{y}{H}, \quad t^* = \frac{t\nu}{H^2}$$

$$u^* = \frac{uH}{\nu}, \quad v^* = \frac{vH}{\nu}, \quad p^* = \frac{pH^2}{\rho\nu^2}$$

$$k^* = \frac{kH^2}{\nu^2}, \quad \epsilon^* = \frac{\epsilon H^4}{\nu^3}, \quad \nu_t^* = \frac{\nu_t}{\nu}$$

$$\rho_s^* = \frac{\rho_s}{\rho}, \quad c_s^* = \frac{c_s}{c_p}, \quad \lambda_s^* = \frac{\lambda_s}{\lambda}$$

$$T^* = \frac{T - T_{\text{in}}}{\Delta T}, \quad \Delta T = \frac{\dot{Q}_v H^2}{\lambda} \tag{13}$$

The relation between the average heat transfer coefficient α based on the maximum temperature of the block and the heat generation rate is as follows:

$$\alpha(H_1 + L_3)(T_{\max} - T_{\text{in}}) = \dot{Q}_v H_1 L_3 \tag{14}$$

Hence the average Nusselt number is given by:

$$Nu \equiv \frac{\alpha H}{\lambda} = \frac{H_1^* L_3^*}{H_1^* + L_3^*}\frac{1}{T_{\max}^*} \tag{15}$$

3.2. Initial and boundary conditions

The initial conditions for the problem are $T^* = u^* = v^* = k^* = \epsilon^* = 0$ throughout computational domain. The hydrodynamic boundary conditions in mixed and forced convection cases for the fluid region ABCDELMNA are zero normal gradients of normal and tangential velocities on the symmetry boundary EL and mass impermeability on the solid boundaries BC, CD, DE and MN, prescribed dimensionless velocity at the inlet AB with time-invariant and rectangular profile and prescribed pressure at the exit LM. On AN, symmetry (Problem 1) or no-slip (Problem 2) conditions are applied. The thermal boundary conditions for the fluid region ABCDELMNA are zero dimensionless temperature at the inlet AB, zero normal gradient of temperature on the EL and AN, zero normal gradient of temperature at the exit LM, no temperature jump and heat flux continuity on the solid–fluid interfaces CD and DE and adiabatic condition on BC and MN. For the solid domain CPEDC, adiabatic conditions are used on the boundaries CP and PE and heat flux continuity with no temperature jump is prescribed on CD and DE.

On solid walls (BC, CD, DE, MN), the condition $k^* = 0$ is applied for all the models. For the standard k–ϵ model (Model 1), the condition $\epsilon^* = (c_\mu^{0.75} k^{*1.5})/(\kappa \Delta_w^*)$ is specified at one point away from the solid wall where Δ_w^* is the distance from the solid wall and $\kappa = 0.41$. In the computations, the first mesh spacing expressed as a friction coordinate is in the viscous sublayer, i.e., $\Delta_w^+ < 5$. For the low Reynolds number model (Model 2), ϵ^* is set to zero on the solid walls. Symmetry boundary conditions are applied on boundary EL for k^* and ϵ^* for Models 1 and 2. At the inlet, small values of turbulent viscosity and turbulent kinetic energy ($\nu_t^* = 0.04, k^*/\nu_{\text{in}}^{*2} = 0.01$) are specified to trigger the turbulence. Gradients of turbulent quantities in the streamwise direction at the outlet are set to zero. While applying boundary conditions to turbulence equations, AN is treated as symmetry boundary for Problem 1 and the same is treated as solid wall for Problem 2.

Table 1
Results of code validation

Turbulent natural convection in a square cavity			
Hot wall *Nu* (adiabatic horizontal walls)			
	$Ra = 10^8$	$Ra = 10^{10}$	$Ra = 10^{11}$
Present solution (Model 1)	33.2484	138.75	315
Present solution (Model 2)	-	101.25	162.89
Markatos and Pericleous [26] (Model 1)	32.045	156.85	341[$]
Henkes et al. [15] (Model 1)	30.831	128.51	320.5
Henkes et al. [15] (Model 2)	–	–	171
Experimental correlation [14] ($Nu = 0.047Ra^{1/3}$)	21.8155	101.25	218
Perfectly conducting horizontal walls (Model 1)			
	Nu_{up}	Nu_{hot}	$\nu^*_{t,max}$
Present solution ($Ra = 6 \times 10^6$)	6.375	12.41	1.08
Fraikin et al. [25] ($Ra = 6 \times 10^6$)	6.339	11.75	3.19
Turbulent mixed convection in a cavity			
	Nu	ψ^*_{max}	$\nu^*_{t,max}$
Present solution ($Re = 1000$, $Ar = 50$) (Model 1)	18.1	1.076	14.8
Present solution ($Re = 1000$, $Ar = 50$) (Model 2)	16.2	1.08	–
P & J [13] ($Re = 1000$, $Ar = 50$) (Model 1)	20.54	1.19	8.2
Present solution ($Re = 2000$, $Ar = 12.5$) (Model 1)	19.4	1.073	15.2
Present solution ($Re = 2000$, $Ar = 12.5$) (Model 2)	17.7	1.074	–
P & J [13] ($Re = 2000$, $Ar = 12.5$) (Model 1)	21.81	1.083	5.2

Model 1: Standard k–ϵ model, Model 2: LS Low-*Re* k–ϵ model.
[$] Calculated from correlation reported in [26].

4. Solution methodology

As mentioned in Bhoite et al. [1], for mixed convection, the dimensionless inlet velocity v^*_{in} is written as:

$$v^*_{in} = Re + v^*_{in,nc} \tag{16}$$

where the Reynolds number *Re* is defined as $v_{in,fc}H/\nu$ ($v_{in,fc}$ being the forced convection inlet velocity) and the dimensionless natural convection inlet velocity $v^*_{in,nc}$ is defined as $v_{in,nc}H/\nu$ ($v_{in,nc}$ being the natural convection inlet velocity in the mixed convection case).

The forced convection velocity $v_{in,fc}$ corresponds to the velocity produced by the fan in isothermal flow and the natural convection velocity $v_{in,nc}$ corresponds to that induced by the buoyancy effect in the presence of mixed convection. It is assumed that mixed convection pressure drop Δp^* (difference in the average pressure between the inlet and the outlet) produced across the enclosure is the same as that produced by forced flow alone and that natural convection, whether acting alone or in the presence of mixed convection, being driven by buoyancy, does not produce any pressure drop. The zero pressure drop assumption for natural convection is applicable when the flow is inducted from and exits into atmosphere or plenums which are essentially at the same pressure. The same methodology was earlier adopted for the laminar mixed convection study reported in Bhoite et al. [1].

To proceed with the solution, first the pure forced convection problem with $v^*_{in} = Re$ and $Gr = 0$ can be solved for various values of *Re* and a correlation can be established between the pressure drop Δp^* and *Re*. The mixed convection problem is then solved for a prescribed dimensionless total inlet velocity v^*_{in} and *Gr*, and the pressure drop Δp^* is determined. Since by assumption, the mixed and forced convection pressure drops are the same for a given Reynolds number, the value of *Re* in mixed convection can be found using the forced convection correlation relating the pressure drop and the Reynolds number. The quantity $v^*_{in,nc}$ (denoting the dimensionless average natural convection inlet velocity in the mixed convection case) can be determined by subtraction, i.e., $v^*_{in,nc} = v^*_{in} - Re$.

The governing equations are solved by an implicit version of the SMAC algorithm [23] with iterative time advancement. The combined convection and diffusion terms are approximated by the power-law scheme [24].

5. Validation and grid sensitivity tests

Computer programs for various models are developed for the present problem based on the discretized governing equations for different turbulence models. The modules of the code are used to reproduce the results for turbulent natural convection in a differentially heated square cavity, which was numerically investigated by Fraikin et al. [25], Henkes [14], Henkes et al. [15] and Markatos and Pericleous [26], and for the problem of turbulent mixed convection in a square cavity, with an isoflux heat source, forming part of the bottom wall of a channel, which was numerically studied by Papanicolaou and Jaluria [13]. The results of validation reported in Table 1 show a good agreement with published k–ϵ model results despite the different numerical formulations (vorticity-stream function versus primitive), solution methodologies and minor differences in turbulence modeling techniques used by the investigators.

The results of the grid independence tests presented in Table 2 for $\lambda^*_s = 10$, $Pr = 0.7$ with the geometrical parameter values $L^*_1 = 0.1$, $L^*_2 = 0.15$, $L^*_3 = 0.25$, $L^*_4 = 0.1$, $H^*_1 = 0.25$, $H^* = 1$ reveal that a near doubling of grid points ($50 \times 50 = 2500$ to $60 \times 75 = 4500$) does not produce any significant differences in the results. Hence a grid of 50×75 non-uniform mesh with larger density of grid points near the boundaries, obtained by the use of Roberts transformation [27], is chosen for subsequent computations as a compromise between accuracy and computing time for Model 1. The jet inlet and outlet regions contain 10 mesh spacings in the horizontal direction for Model 1. The transformation facilitates generation of suitable meshes to capture the essential near-wall dynamics as per the requirement of different turbulence models, with the help of the grid stretching parameter. For instance, a very fine mesh is required to implement the Yap correction with the node adjacent to the boundary deployed at a dimensionless distance of 5×10^{-4}; to satisfy the criteria $\Delta^+_w \leqslant 0.1$ applicable to first grid point away from the wall. To facilitate computations with Model 2, a grid of 60×75 is selected with the jet

Table 2
Results of grid sensitivity tests

Grid size[+]	Problem 2, Model 1			
	$v^*_{in} = Re = 3 \times 10^5$, $Gr = 0$ (FC)		$v^*_{in} = 7 \times 10^5$, $Gr = 10^{15}$ (MC)	
	Eu	$100T^*_{max}$	Eu	$100T^*_{max}$
40×40	0.5040	0.3800	0.5100	0.3550
50×50	0.6029	0.3337	0.6453	0.2988
50×75	0.5694	0.2890	0.6126	0.2690
60×75	0.5526	0.2840	0.6253	0.2638

[+] Number of control volumes in x^* and y^* directions, respectively. $Eu = \Delta p^*/Re^2$, FC: Forced Convection, MC: Mixed Convection.

inlet and outlet regions covered with 12 spacings each in the horizontal direction. Meshes finer than 60×75 are also tried and it is found that more refinement did not improve the results much.

6. Results and discussion

Results are obtained for various values of Reynolds and Grashof numbers, for $\lambda^*_s = 10$, $Pr = 0.7$, with the turbulence models, for the geometrical parameter values mentioned earlier.

6.1. Pressure drop in forced convection

The variation of the Euler number ($Eu = \Delta p^*/Re^2$) with Reynolds number is depicted in Fig. 2. As revealed by the figure, there is a jump with about 30 per cent rise in friction factor as the flow changes from laminar to turbulent regime. In [1], laminar flow solutions for forced convection were reported for $Re < 5000$. For Reynolds numbers in the range 5000 to 10^5, the laminar model does not converge to a steady solution but gives oscillatory periodic solutions for the range 5×10^3–10^4 and oscillatory aperiodic solutions for the range 10^4–10^5. Beyond $Re = 10^5$, converged solutions with laminar model could not be obtained. Moreover, turbulent flow computations with Models 1 and 2 yielded oscillatory periodic solutions in the range of Reynolds number 10^4–5×10^5 and 10^4–10^7, respectively.

The results obtained with the standard k–ϵ show that the Euler number increases rapidly after $Re = 10^4$. This behavior can be seen in Fig. 2(a) (Problem 1) and Fig. 2(b) (Problem 2). Further, in the range $10^4 < Re < 5 \times 10^5$, as mentioned earlier, the turbulent computations yielded oscillatory solutions with non-zero turbulent quantities. Fully turbulent steady solutions could be obtained for Reynolds numbers above 5×10^5. The values of Eu plotted in Figs. 2(a) and 2(b) for $10^4 < Re < 5 \times 10^5$ are the mean values.

The Launder–Sharma model predicted lesser pressure drop compared to the standard k–ϵ model. Computations with Model 2 showed similar behavior for Problem 2 except that the oscillatory state extended till $Re = 10^7$ beginning from $Re = 10^4$. Computations with and without Yap correction term have shown that the Yap correction generally improves the convergence. However for Problem 1, which involves free boundaries, no significant differences are obtained in the results obtained by Models 1 and 2.

Pressure drop correlations for the turbulent regime are presented in Table 3. The pressure drop for non-partitioned enclosure (Problem 1) is higher than that for the partitioned enclosure (Problem 2) by about 25 per cent. The reason is traced to the fact that the solid partitions create circulations at the top corners diverting the main flow towards the outlet, while this mechanism is absent in the case of the enclosure with free boundaries. This can be seen from Fig. 3, in which the streamline and isotherm patterns for pure forced convection at $Re = 10^7$ (using Model 1) are presented. Due to the large magnitude of ψ^*, in the streamline maps, the contour values are shown for the dimensionless stream function divided by a factor of 100. The isotherms are presented in the form of contours of $\log_{10} T^*$ to take into account smaller values of T^* also. Figs. 3(a) and 3(b) apply to Problem 1 and Problem 2, respectively. Results with Model 2 exhibited similar contour patterns for the stream function and temperature.

Table 3
Pressure drop correlations

Correlation	SEE	CC	Range
	Problem 1, Model 1		
$\Delta p^* = 0.6029\,Re^2$	6×10^{-5}	0.999	$5 \times 10^4 \leqslant Re \leqslant 10^6$
	Problem 2, Model 1		
$\Delta p^* = 0.5058\,Re^{2.01}$	0.0041	0.999	$10^4 \leqslant Re \leqslant 10^6$
	Problem 1, Model 2		
$\Delta p^* = 0.6032\,Re^2$	4×10^{-5}	0.999	$5 \times 10^4 \leqslant Re \leqslant 10^6$
	Problem 2, Model 2		
$\Delta p^* = 0.9078\,Re^{1.96}$	0.001	0.999	$10^4 \leqslant Re \leqslant 10^6$

SEE = Standard Error of Estimate, CC = Correlation Coefficient.

Table 4
Threshold Reynolds number (Re_{turb}) values for turbulent solutions for various Gr

Gr	Re_{turb}
Problem 1 (Model 1)	
0	5×10^5
10^{14}	4.81×10^5
10^{15}	4.56×10^5
Problem 2 (Model 1)	
0	5×10^5
10^{10}	4.5×10^5
10^{15}	4.312×10^5
Problem 2 (Model 2)	
0	10^7
10^{15}	$\approx 10^7$

6.2. Ranges of governing parameters for turbulent regime

Based on the numerical data obtained from several runs, values of the governing parameters at which the flow turns to be turbulent for the given geometry and for a fixed Prandtl number ($Pr = 0.7$) are identified and are listed in Table 4. For $Re \geqslant Re_{turb}$, significant turbulence ($\nu^*_t \geqslant 10$) is seen in the solution. It can be observed that the model employed influences the limiting values.

However, higher Grashof numbers lower the value of Re_{turb} slightly due to buoyancy-induced instabilities, as can be seen from Table 4. Turbulent solutions with Model 2 could be obtained only for $Re \geqslant 10^7$ for any Grashof number. To see the effect of higher Grashof number at $Re = 10^7$, computations were carried out with $Gr = 10^{15}$. Although this case was successfully computed, the parameter values themselves are on the much higher side when considering applications like conditioned enclosures and electronic cooling problems. Since with Model 2, the placement of the first grid point should be such that $\Delta^+_w \leqslant 0.1$, there was already a requirement for a very fine mesh at $Re = 10^7$ for the implementation of the Yap correction with the node adjacent to the boundary deployed at a dimensionless distance of 5×10^{-4}. Further grid refinement for still higher parameter values presented convergence problems.

6.3. Natural convection

To solve the pure natural convection problem, the dimensionless inlet velocity that results in zero Δp^* across the enclosure is determined for a given Grashof number. The values of the pure natural convection inlet velocity $v^*_{in,pnc}$ are presented in Table 5.

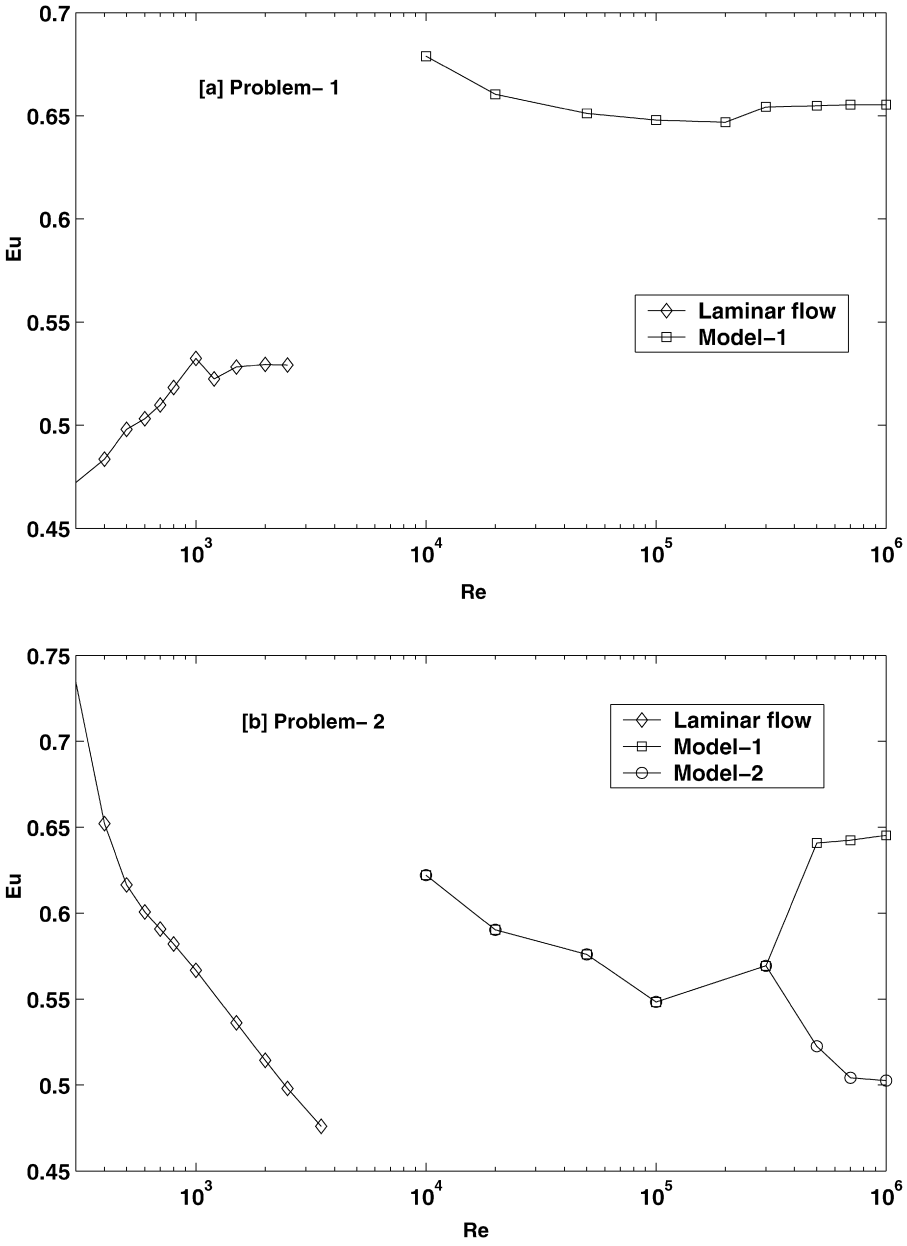

Fig. 2. Variation of Euler number with Reynolds number.

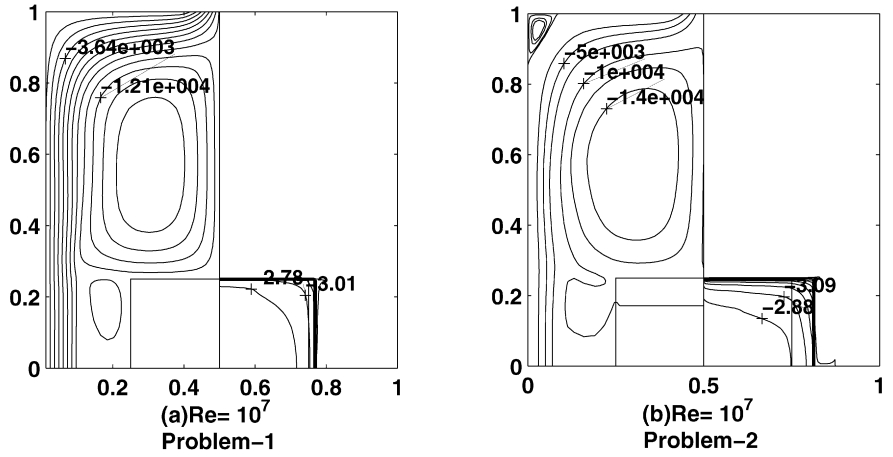

Fig. 3. Streamlines (left) and isotherms (right) for pure forced convection for ($Re = 10^7$). (a) Problem 1, (b) Problem 2.

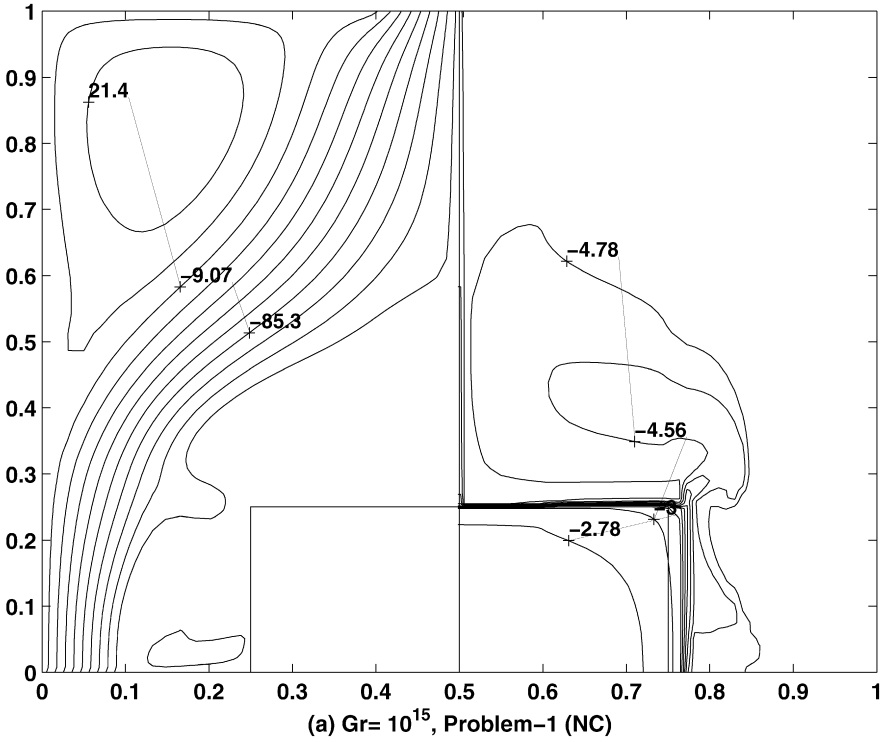

Fig. 4. Streamlines (left) and isotherms (right) for pure natural convection for ($Gr = 10^{15}$) (Problem 1).

Table 5
Dimensionless natural convection inlet velocities

Gr	$v^*_{\text{in,pnc}}$	
	Problem 1	Problem 2
10^{11}	6.9×10^3	6.7×10^3
10^{12}	1.475×10^4	1.554×10^4
10^{13}	3.2×10^4	3.35×10^4
10^{14}	6.87×10^4	7.5×10^4
10^{15}	1.3×10^5	1.558×10^5

The results are obtained for the Grashof number range $10^{10} \leqslant Gr \leqslant 10^{15}$. However, in this range, the oscillatory solutions are found for both Problems 1 and 2. The solutions have not shown any significant level of turbulence with either model. The results presented here are for time-averaged quantities corresponding to the 50×75 grid mentioned earlier. The results for the maximum temperature in pure natural convection can be of help in judging the efficacy of cooling in the mixed convection regime.

From the values presented in Table 5, it is observed that the quantity $v^*_{\text{in,pnc}}$ varies as $Gr^{1/3}$. For pure natural convection problem, both the models yielded laminar reverted solutions.

Pure natural convection streamline and isotherm patterns for $\psi^*/100$ and $\log_{10} T^*$ are shown in Fig. 4 for $Gr = 10^{15}$ for Problem 1. For Problem 2, the flow and temperature distributions are found to be nearly the same. Since the computations with turbulent models reverted to laminar regime, no comparison is made between Models 1 and 2. Compared to the case of forced convection, the streamlines for pure natural convection reveal that the entering stream is bent towards the block because of the buoyancy force, resulting in a bigger recirculation zone near the top corners.

6.4. Effect of natural convection on the inlet velocity

The dimensionless total inlet velocity v^*_{in} in mixed convection is plotted against the Reynolds number ($= v_{\text{in,fc}} H/\nu$) in Fig. 5 for various values of Grashof number, for Model 1 with the subfigures applicable to Problems 1 and 2. For any Grashof number, it can be seen that for lower values of Re, the quantity v^*_{in} is larger than Re. This is because at lower Reynolds numbers, the buoyancy contributes significantly to the forced flow effect, drawing extra amount of fluid into the enclosure. It is not difficult to see that the contribution of buoyancy to the total inlet velocity increases with increasing Grashof number. For the range of Grashof numbers 10^{12}–10^{15}, the buoyancy effect is found to become negligible beyond a Reynolds number of 5×10^5. Thus beyond this limit, the total inlet velocity becomes almost equal to the Reynolds number.

An idea of the relative strengths of buoyancy and inertia forces can be obtained from the ratio $v^*_{\text{in}}/Re = (v^*_{\text{in,nc}} + Re)/Re$ (the ratio of the total inlet velocity in mixed convection to that induced by fan). The ratio v^*_{in}/Re becomes ∞ for pure natural convection ($Re = 0$) and unity for pure forced convection ($v^*_{\text{in,nc}} = 0$). Fig. 5 shows that v^*_{in}/Re begins to approach unity for $Re \geqslant 5 \times 10^5$.

6.5. Streamlines and isotherms for mixed convection

The streamline and isotherm contours for pure forced and pure natural convection are already presented in Figs. 3 and 4. Selected streamline and isotherm maps for mixed convection are shown in Fig. 6 (Problem 1, $Gr = 10^{14}$, Model 2), Fig. 7 (Problem 2, $Gr = 10^{14}$, Model 1) and Fig. 8 (Problem 2, $Gr = 10^{15}$, Model 1) with the subfigures applicable to different Reynolds numbers. The contour values shown are for $\psi^*/100$ and $\log_{10} T^*$. The streamline and isotherm maps for each Grashof number show the general features of the flow and temperature fields.

By comparing Figs. 6–8 with Figs. 3 and 4, the change from natural convection dominated regime to forced convection dominated regime can be clearly discerned. The waning off of the buoyancy effects with increasing Re can be seen by proceeding from subfigure (a) to subfigure (f) in Figs. 6–8.

The streamlines obtained in turbulent flow are found to be qualitatively similar to those obtained for laminar flow. In case of Problem 1 (i.e., enclosure with free boundaries), a strong recirculation is observed above the top face of the block. In addition, a

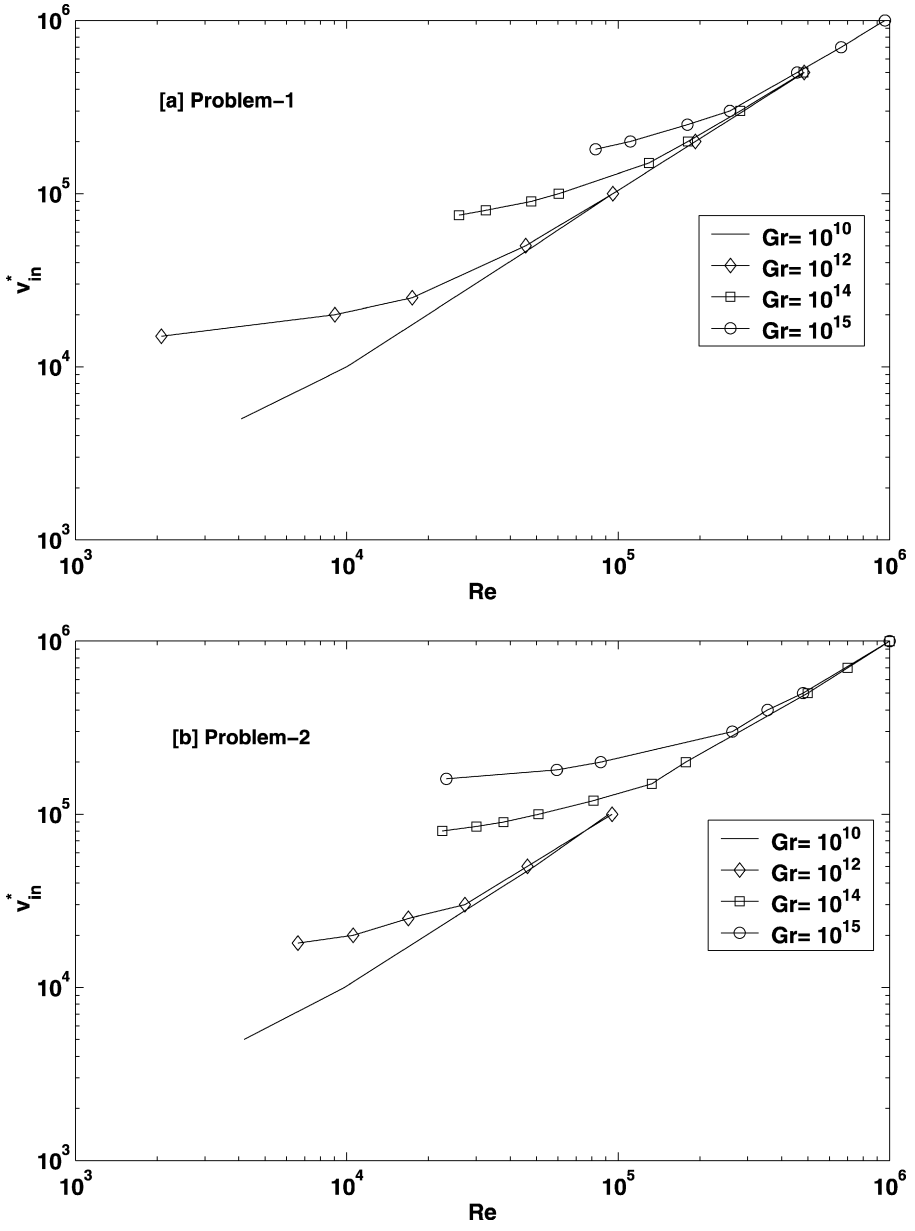

Fig. 5. Variation of the total inlet velocity with the Reynolds number for Model 1. (a) Problem 1, (b) Problem 2.

weak recirculation zone is observed at the sides of vertical faces. For Problem 2 (fully partitioned enclosure), a recirculation zone is observed at the top corners directly above the inlet streams. It can be seen that buoyancy tends to deflect the fluid towards the block by creating a low pressure zone locally.

The isotherms are clustered in the fluid region adjacent to the solid–fluid interface because of the high solid-to-fluid thermal conductivity ratio and relatively lower fluid velocities in this region.

6.6. Distribution of turbulent viscosity and kinetic energy

Fig. 9 depicts the spacewise distribution of dimensionless turbulent kinetic energy and dimensionless turbulent viscosity for $Gr = 10^{15}$ with different subfigures applicable to different Reynolds number and turbulence models. The quantities $\log_{10} k^*$ and $\log_{10} \nu_t^*$ are chosen for the display of contours to capture the wide variation of these variables. Figs. 9(a) and 9(b) correspond two different Reynolds numbers.

Results with Model 1 depicted in Figs. 9(a) and 9(b) reveal that k^* and ν_t^* are higher in the corners than in the core region. This means that turbulence is originated from the high shear rate due to flow and wall interaction. Model 1 does not predict any significant turbulence in the recirculating region of the core.

Fig. 10 shows the spacewise distribution of dimensionless turbulent kinetic energy and dimensionless turbulent viscosity for $Gr = 0$, $Re = 10^7$ for Models 1 and 2. The quantities $\log_{10} k^*$ and $\log_{10} \nu_t^*$ are chosen for the display of contours to capture the wide variation of these variables. Figs. 10(a) and 10(b) apply to Models 1 and 2, respectively. As can be seen, Model 2 predicts turbulence in the recirculating core while Model 1 does not. Both models show turbulence in the vicinity of the top wall.

Fig. 11 shows profiles of u^+ $(= u/u_*)$, k^+ $(= k/u_*^2)$ and ν_t^+ $(= \nu_t/u_* H)$ against the friction coordinate Δ_w^+ $(= \Delta_w u_*/\nu)$ measured from the top wall for $Gr = 0$, $Re = 10^7$ at $x^* = 0.2$ for Models 1 and 2. Regions near the corners are chosen for plotting since more turbulence is developed in the corners. The corresponding streamline and isotherm patterns for this case are depicted in Fig. 3. Fig. 11(a) shows dimensionless wall scaled velocity profile from $y^+ = 0$ (wall) to $y^+ = 100$ and the graph shows that lin-

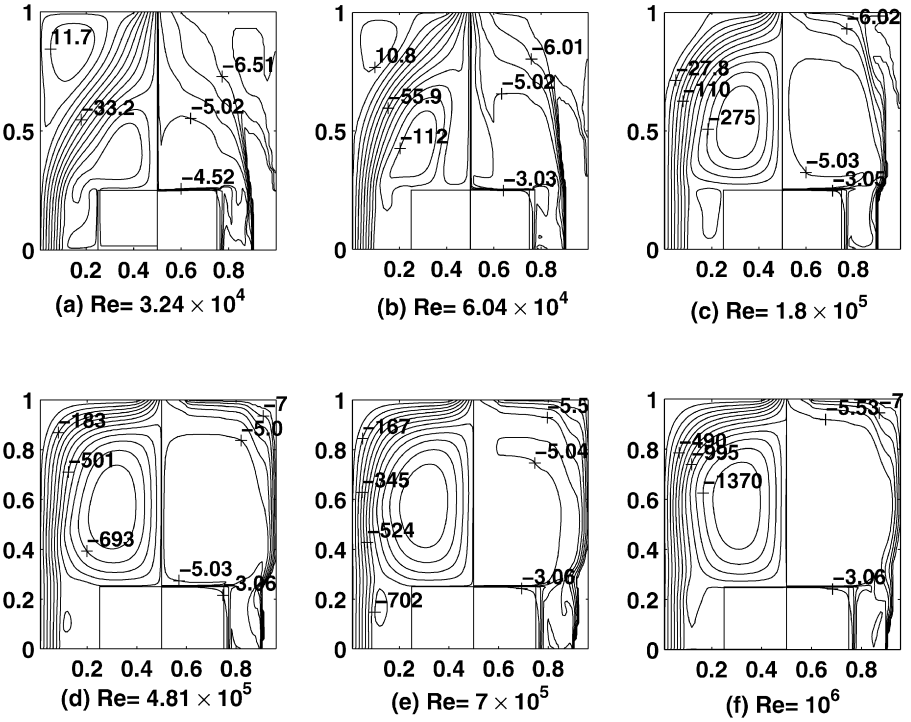

Fig. 6. Streamlines (left) and isotherms (right) for $Gr = 10^{14}$ (Problem 1, Model 2).

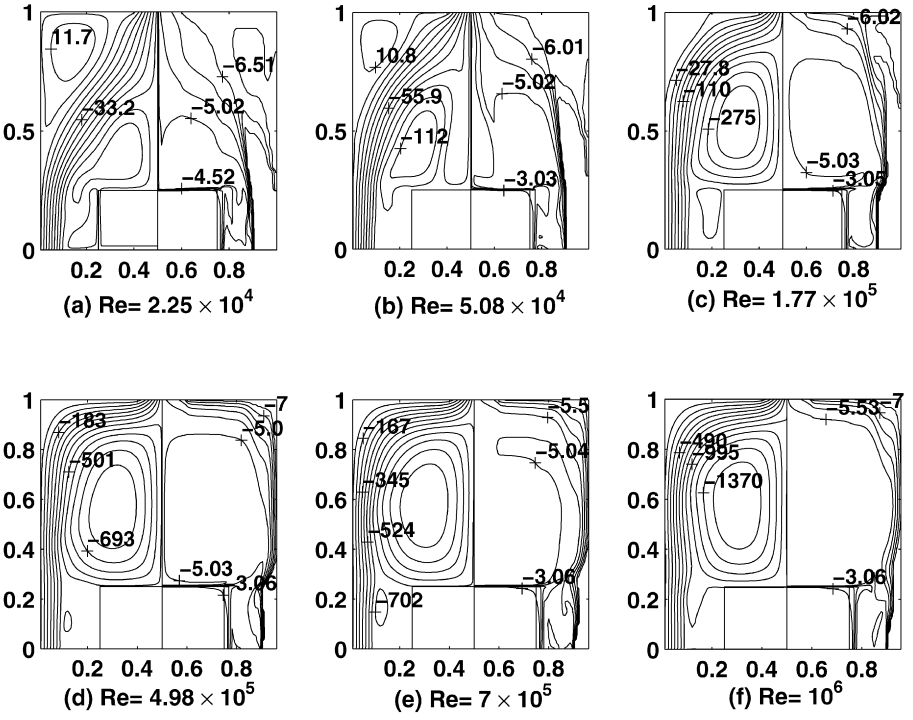

Fig. 7. Streamlines (left) and isotherms (right) for $Gr = 10^{14}$ (Problem 2, Model 1).

ear and log law profiles are well followed since the flow pattern at $x^* = 0.2$ (as can be seen from Fig. 3) is similar to boundary layer flow pattern. It can be observed from Fig. 11(b) that near the wall the turbulent kinetic energy attains a high value, i.e., there is steep rise in k^+ as the fully turbulent layer is approached from the wall. Beyond this point, k^+ rapidly decreases because the mean shear decreases. The variation of ν_t^+ is slightly more complicated in that it may have single or multiple peaks. Beyond the peaks, the quantity ν_t^+ decreases rapidly. In a boundary-layer type flow, the quantity ν_t^+ attains a peak and then decreases. However, in the present problem, the near-wall flow is not of boundary-layer type and is influenced by the recirculation zones and the flow near the enclosure exit. The turbulence levels predicted by Model 2 are lower than those predicted by Model 1.

It is observed that the flow in the fully partitioned enclosure (Problem 2) has much higher turbulence than that of the free boundary enclosure (Problem 1). The reason is that in Problem 1, the flow entering the enclosure gives rise to a jet-like structure

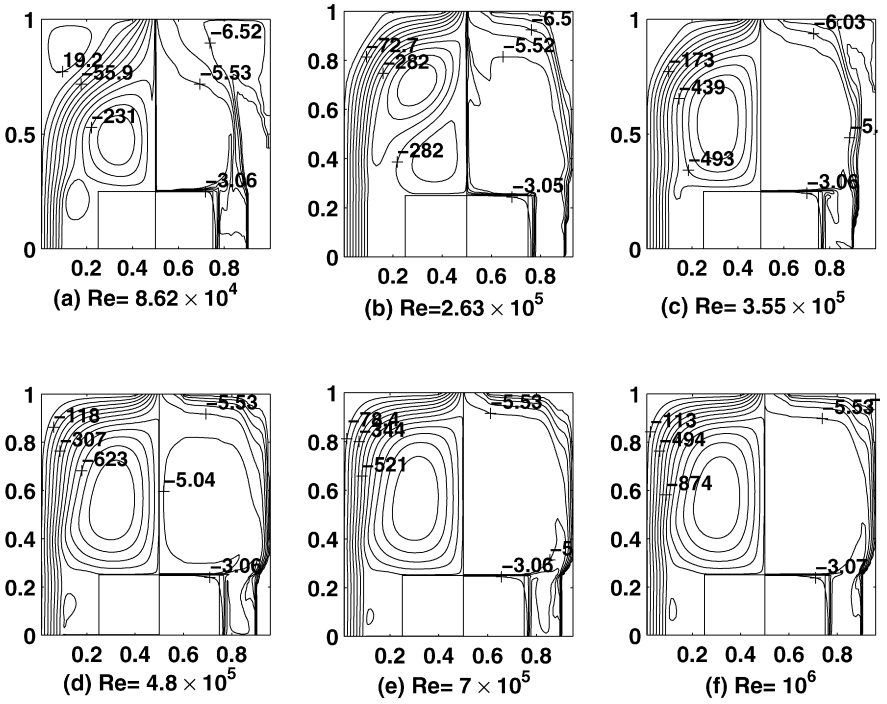

Fig. 8. Streamlines (left) and isotherms (right) for $Gr = 10^{15}$ (Problem 2, Model 1).

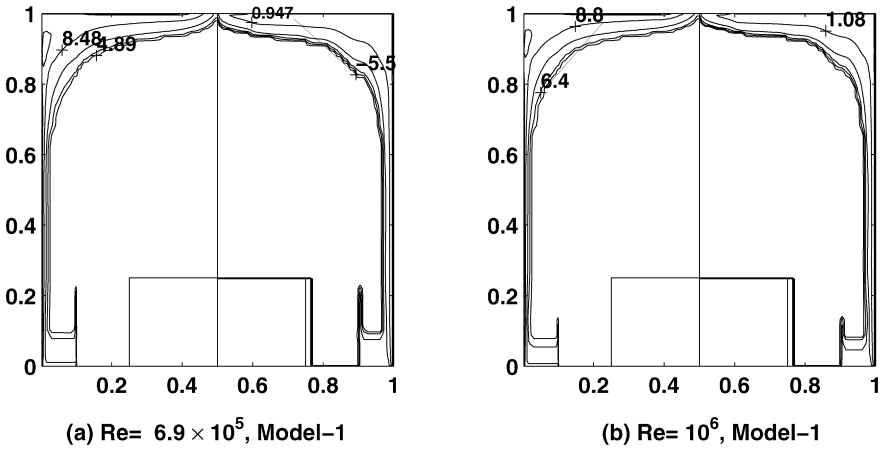

Fig. 9. Contours of turbulent kinetic energy (left) and turbulent viscosity (right) for Problem 2, for $Gr = 10^{15}$.

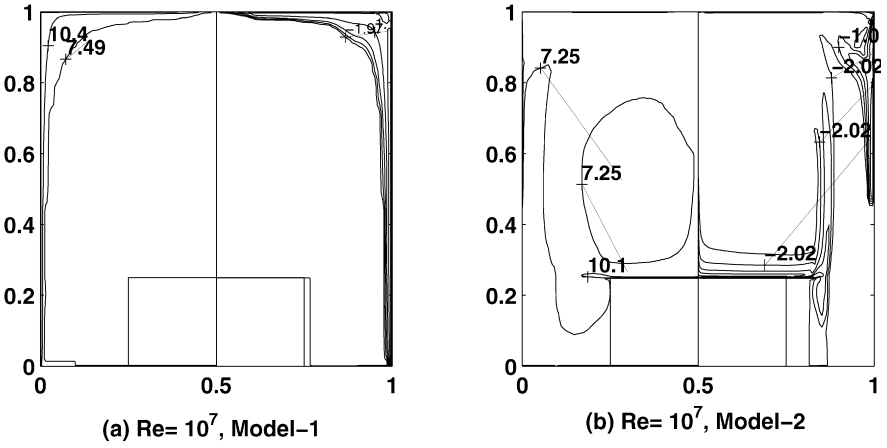

Fig. 10. Contours of turbulent kinetic energy (left) and turbulent viscosity (right) for Problem 2, for $Re = 10^7$; $Gr = 0$. (a) Model 1, (b) Model 2.

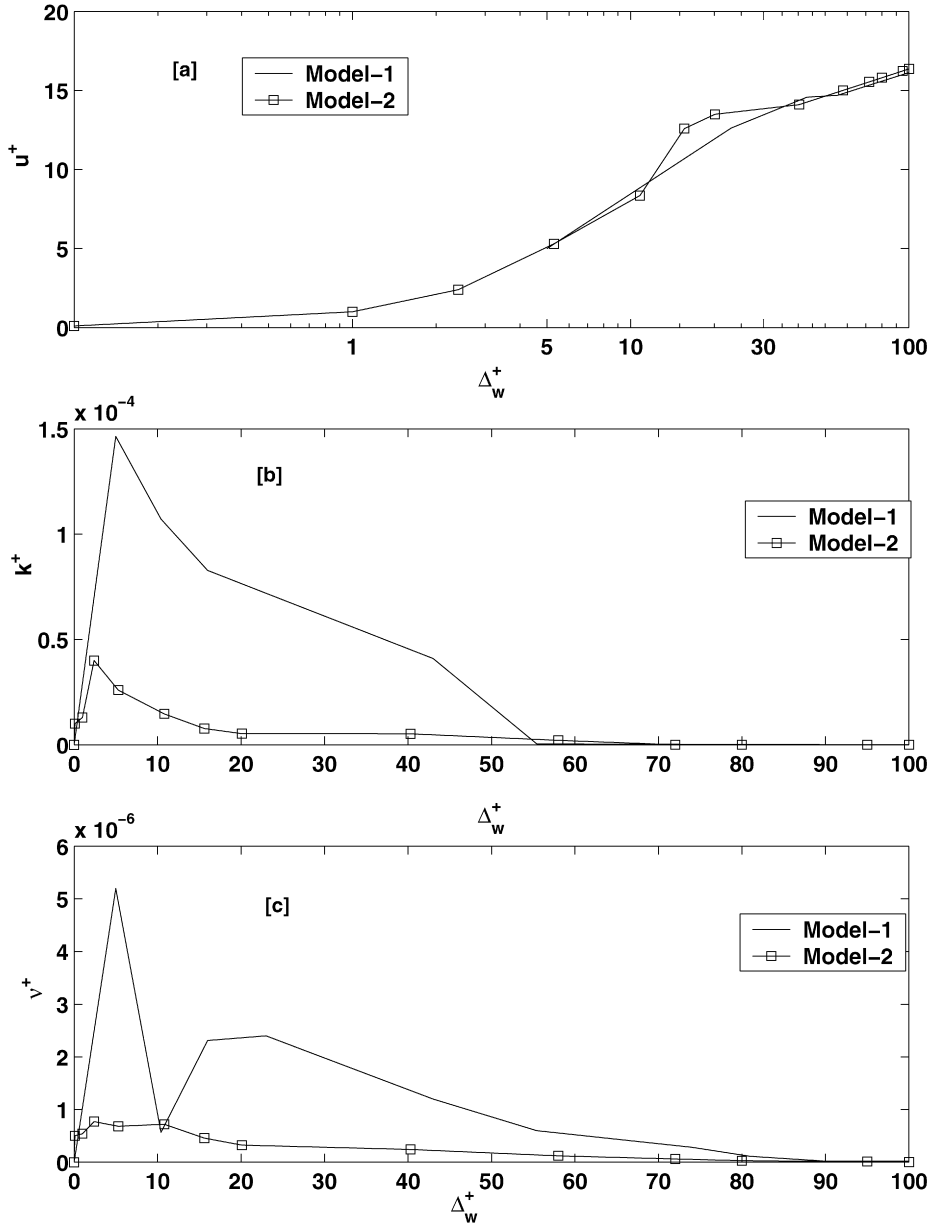

Fig. 11. Near wall profiles of turbulent variables for Problem 2 with Model 1 and Model 2 ($Re = 10^7$; $Gr = 0$) at $x^* = 0.2$ for Problem 2.

with lower shear compared to the wall-bounded flow in Problem 2 where high shear rate regions act as sources of turbulent production of kinetic energy.

6.7. Maximum temperature and Nusselt number

Fig. 12 shows the variation of maximum dimensionless temperature with *Re* and *Gr*, respectively for Model 1. The maximum dimensionless temperature decreases with increase in Grashof number. However, such a reduction does not mean that maximum dimensional temperature drops with a rise in the volumetric heat generation. Rather, it indicates that the rate at which the maximum temperature increases is less compared to that in the volumetric heat generation rate. The maximum dimensionless temperature can also be seen to decrease with an increase in Reynolds number, barring the lower Reynolds number region where overheating of the block can occur.

Since the Nusselt number, by definition, is proportional to the reciprocal of maximum dimensionless temperature, its variation is just opposite to that of T^*_{max} as depicted in Fig. 13, where it can be observed that the Nusselt number, in general, increases with increase in Reynolds and Grashof numbers.

Table 6
Comparison of T^*_{max} between Models 1 and 2

Re	*Gr*	$100T^*_{max}$		Change
		(Model 1)	(Model 2)	(%)
5×10^5	0	0.2781	0.2919	4.96
7×10^5	0	0.2728	0.2793	2.382
7×10^5	10^{15}	0.28	0.2863	2.25
10^6	0	0.2692	0.2799	3.974
10^6	10^{15}	0.2674	0.2790	4.33
10^7	0	0.26	0.2108	23.80[$]

[$] Model 2 switches to fully turbulent regime.

Values for maximum dimensionless temperature obtained with Model 2 differ by 5 to 10 per cent from those obtained by Model 1 for $v^*_{in} \leqslant 10^6$. Table 6 shows the comparison of selected maximum dimensionless temperatures obtained for Problem 2 using Mod-

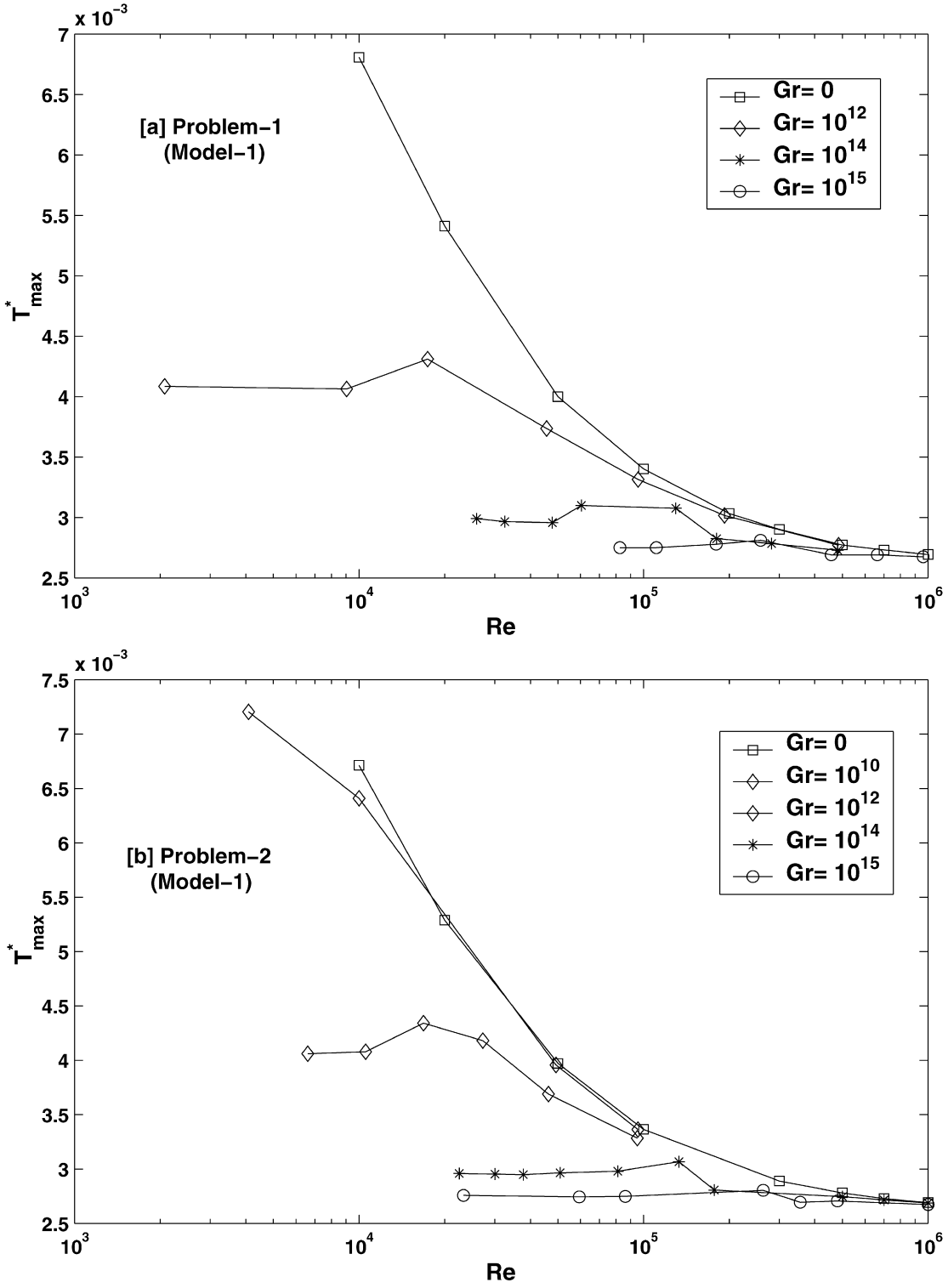

Fig. 12. Variation of maximum dimensionless temperature with Reynolds number for various Grashof numbers (Model 1).

els 1 and 2. The values obtained by the low Reynolds number model (Model 2) are about 5 per cent higher than those obtained by the standard k–ϵ model (Model 1) for $Re < 10^7$. Despite the differences in the turbulence levels predicted by Models 1 and 2, the difference in the maximum dimensionless temperature is not significant for $Re < 10^7$ because adjacent to the block surface ν_t^* is insignificant. However, the difference in T^*_{max} between Model 1 and Model 2 turns out to be more than 20 per cent at $Re = 10^7$, i.e., when Model 2 yields a fully turbulent solution. At this Reynolds number, the convective flow regime is dominated by forced convection.

The maximum dimensionless temperature obtained for Problems 1 and 2 with the standard k–ϵ model, for a given value of total inlet velocity, differs at the most by 10 per cent at lower values of ν^*_{in} (typically 10^4). The difference tends to diminish as ν^*_{in} increases; for instance, at $\nu^*_{in} = 10^6$, negligible difference is observed between the maximum dimensionless temperature for Problems 1 and 2. With either model, for Reynolds number greater

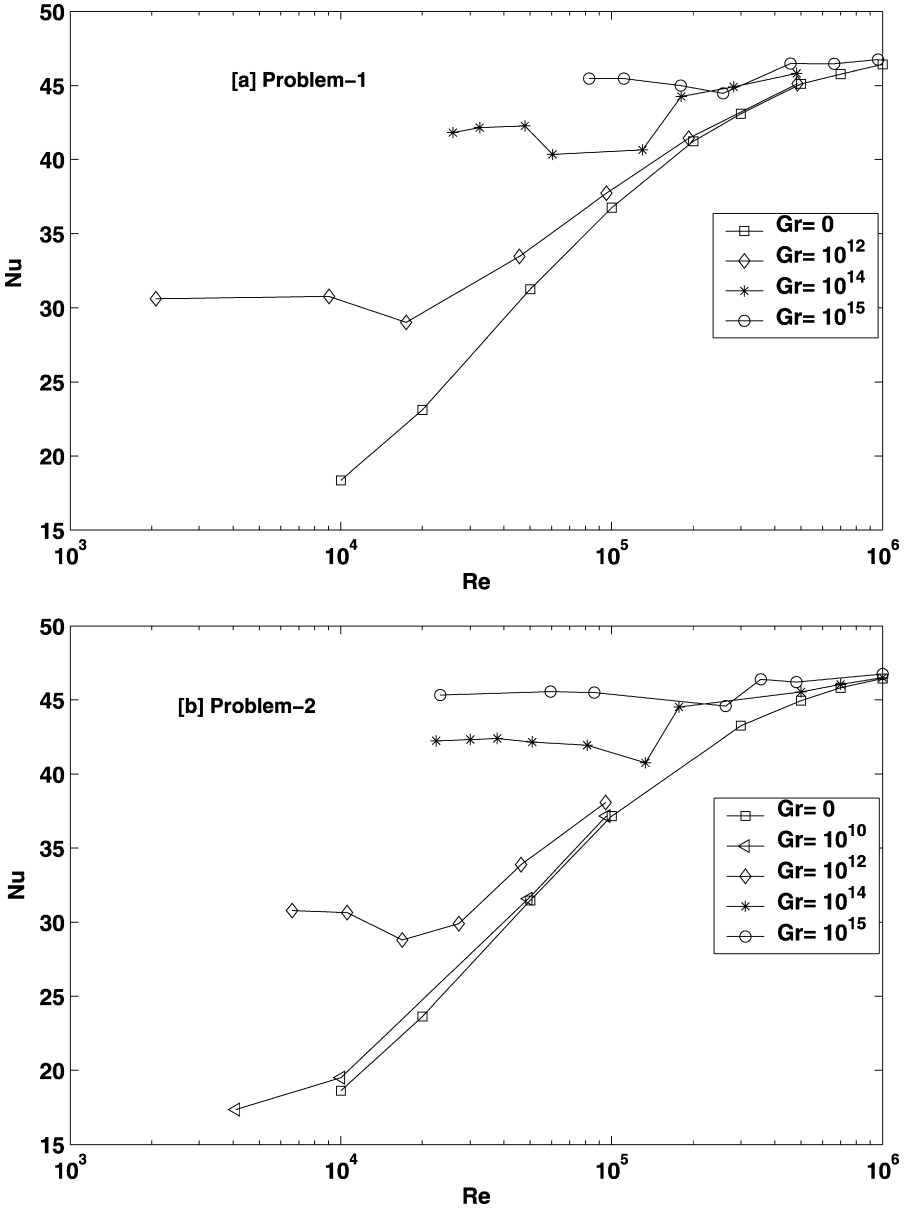

Fig. 13. Variation of Nusselt number with Reynolds number for various Grashof numbers (Model 1).

than 5×10^5, the maximum dimensionless temperature becomes independent of the Grashof number.

To have an estimate of the dimensional temperatures obtained by Model 1, let the geometry represent an enclosure of height 3 m with other relative dimensions as chosen in the present study without partitions (Problem 1). For a Grashof number of 10^{14}, the volumetric heat generation will be 72 W per m^3 (8.1 W per meter depth of the block). For this enclosure, for a $v_{in}^* = 10^5$, the total dimensional inlet velocity will be 0.5 $m\,s^{-1}$ and the fan velocity turns out to be 0.25 $m\,s^{-1}$. For a supply air temperature of 20 °C, the maximum dimensional temperature comes to 96 °C (with a difference of 76 °C between the maximum temperature and the supply air temperature). For the same Grashof number and dimensionless total inlet velocity, the dimensional velocities and maximum temperature for the partitioned enclosure (Problem 2) too are almost the same. This example shows that better cooling of the heat generating element is required by an increase of the forced convection velocity or a decrease in the volumetric heat generation, since an operating temperature of 96 °C can go beyond the acceptable limit. The example also shows that the parameter ranges chosen are relevant to practical applications like computer centres. The present analysis can be extended for different arrangements of heat source and cooling jets for resulting into better control over maximum temperature. With Model 2, the quantity $T_{max} - T_{in}$ is found to be higher by about 5 per cent compared to Model 1.

7. Comparison of standard and low Reynolds number models

For Problem 2, the dimensionless pressure drop obtained by Model 2 is higher than that obtained by Model 1 for $Re < 10^5$; the opposite is true for $Re > 10^5$. The difference in the pressure drop can be attributed to the difference in the levels of ν_t^* predicted by the two models.

For Problem 1, the differences between the results obtained by Models 1 and 2 are found to be insignificant. This could be due to the fact that solid–wall partitioning between the modules is absent in Problem 1. In the range $10^4 \leqslant Re \leqslant 5 \times 10^6$, T_{max}^* obtained is insensitive to the model used. At $Re = 10^7$, T_{max}^* obtained by Model 2 is significantly lower than that obtained by Model 1. The

reason can be traced to the fact that at $Re = 10^7$, Model 2 shows turbulence near the block surfaces unlike Model 1, which can also be observed from Fig. 10. Since Model 2 produces turbulence near the block, T^*_{max} is lowered.

Table 7 lists the maximum values of k^* and ν_t^* and their locations for various Reynolds and Grashof numbers computed with different turbulent models. It can be inferred that with an increase in Reynolds number, there is an increase in k^*_{max} and $\nu^*_{t,max}$. However the trend reverses with respect to the Grashof number. Increase in Grashof number deflects the fluid from inlet to the core region above the block due to increased buoyancy. This results in an increased size of the recirculation zones near the top corners and a drop in the mean shear in the corner regions. Consequently, near the top wall, the turbulence production is reduced with increase in Grashof number. However, Grashof number does not influence $\nu^*_{t,max}$ to the extent the Reynolds number does. This is due to the fact that in the regions where k^* and ν_t^* are high, the gradients of temperature are almost zero and the buoyancy production of turbulent kinetic energy (G_k^*) is insignificant in these regions. As can be expected, turbulence increases rapidly with increase in Reynolds number. It is also seen that the locations of turbulent kinetic energy maxima and turbulent viscosity maxima are different from each other. This is attributed to the fact that the production and dissipation of turbulent kinetic energy does not necessarily occur at the same location. For example, the value of $\nu^*_{t,max}$ for $Re = 10^7$ with Model 2 is lower that for $Re = 10^6$ computed with the standard k–ϵ model.

8. Correlations

Correlations are constructed from the computed data for various dimensionless quantities, namely, the pressure drop, maximum temperature and the natural convection inlet velocity in terms of the Reynolds and Grashof numbers and are presented in Table 8, along with the values of the standard error of estimate and multiple correlation coefficient for Model 1. Since, in the ranges relevant to practical applications, Model 2 results are not much different from those obtained by Model 1, separate correlations are not given for Model 2. The standard error of estimate (referred to as SEE)is defined as [sum the squares of error/$(l-m-1)$]$^{1/2}$, where l is the number of data points, m is the number of independent variables and $l-m-1$ is the number of degrees of freedom. The multiple correlation (referred to as CC) is defined as [1 − (sum of squares of residuals/total sum of squares)]$^{1/2}$.

To obtain an estimate of the relative strengths of buoyancy and inertia forces in mixed convection, the ratio $v^*_{in}/Re \equiv (v^*_{in,nc} + Re)/Re$ (the ratio of the total inlet velocity in mixed convection to that induced by fan) can be presented in terms of the Archimedes number Ar ($= Gr/Re^2$). For instance, the correlation for $v^*_{in,nc}$ in the range $0.37 \leqslant Ar \leqslant 2.5 \times 10^5$ for Problem 1 (with Model 1 results) is:

$$\frac{v^*_{in,nc} + Re}{Re} = 8.6616 \frac{Ar^{0.0654}}{Re^{0.46}} \tag{17}$$

The correlation for v^*_{in}/Re for Problem 2, presented in Table 8 and which has the same range of applicability, can be readily transformed to the above form. The correlation for T^*_{max} is expressible in terms of v^*_{in}. Although the Archimedes number is introduced in the above correlations, for problems involving complex geometries and heat generation such as the present one, where the pressure drop is linked to the Reynolds number, there is need to establish more general criteria than the Archimedes number for the demarcation of the regimes.

For the correlations presented in Table 8, the ranges are indicated in terms of Gr and Re, as they encompass all the regimes, namely, the natural, forced and the mixed convection.

9. Conclusions

A computational study of turbulent mixed convection in a shallow enclosure with or without partitions and with block-like heat generating components and inlet and outlet openings is performed by neglecting the end effects and taking into account similar geometric modules and the symmetry in the geometry. The Reynolds number is based on the forced velocity component produced by the fan. This gives the Reynolds number strictly its forced convection attribute unlike the definitions in which the characteristic velocity is taken as the combined natural and forced convection components.

Steady turbulent solutions for forced convection are obtained with standard k–ϵ model at Reynolds numbers higher than 5×10^5 and with low-Reynolds number model for $Re \geqslant 10^7$. The Euler number at these Reynolds numbers is higher by about 30 per cent

Table 7
Magnitudes and locations of the maximum turbulent viscosity and the maximum turbulent kinetic energy (Problem 2)

Re	Gr	$\nu^*_{t,max}$, (x^*, y^*)	k^*_{max}, (x^*, y^*)
		Model 1	
5×10^5	0	289.49 (0.0064, 0.918)	4.032×10^{10} (0.3865, 0.9983)
10^6	0	509.63 (0.0064, 0.93)	1.651×10^{11} (0.3865, 0.9983)
10^7	0	1575.1 (0.3867,0.9987)	1.74×10^{13} (0.3867, 0.9987)
7×10^5	10^{15}	380.53 (0.0156, 0.93)	7.526×10^{10} (0.3865, 0.9983)
7×10^5	10^{14}	385.90 (0.0156, 0.93)	7.791×10^{10} (0.3865, 0.9983)
		Model 2	
10^7	0	448.37 (0.388, 0.9994)	7.6×10^{12} (0.388, 0.9994)

Table 8
Correlations obtained from regression analysis

Regime	Variable	Correlation	SEE	CC	Range
		Problem 1, $\lambda^*_s = 10$, Model 1			
FC	T^*_{max}	$0.0379\,Re^{-0.2}$	0.009	0.97	$5 \times 10^4 \leqslant Re \leqslant 10^6$
NC	$v^*_{in,pnc}$	$2.022 Gr^{0.32}$	0.003	0.999	$10^{10} \leqslant Gr \leqslant 10^{15}$
NC	T^*_{max}	$0.0191\,Gr^{-0.056}$	0.012	0.993	$10^{10} \leqslant Gr \leqslant 10^{15}$
MC	$v^*_{in,nc}$	$8.6616\,Re^{0.67} Gr^{0.0654} - Re$	0.0506	0.98	$10^4 \leqslant Re \leqslant 10^6$ $10^{10} \leqslant Gr \leqslant 10^{15}$
MC	T^*_{max}	$0.0103\,v_{in}^{*\,-0.1}$	0.0013	0.93	same as for $v^*_{in,nc}$
		Problem 2, $\lambda^*_s = 10$, Model 1			
FC	T^*_{max}	$0.0354\,Re^{-0.194}$	0.0091	0.97	$10^4 \leqslant Re \leqslant 10^6$
NC	$v^*_{in,pnc}$	$1.13\,Gr^{0.35}$	0.002	0.999	$10^{10} \leqslant Gr \leqslant 10^{15}$
NC	T^*_{max}	$0.043\,Gr^{-0.081}$	0.012	0.98	$10^{10} \leqslant Gr \leqslant 10^{15}$
MC	$v^*_{in,nc}$	$1.218\,Re^{0.61} Gr^{0.15} - Re$	0.0516	0.98	$10^4 \leqslant Re \leqslant 10^6$ $10^{10} \leqslant Gr \leqslant 10^{15}$
MC	T^*_{max}	$0.0143\,v_{in}^{*\,-0.125}$	0.0027	0.95	same as for $v^*_{in,nc}$

than that in the laminar regime. The pressure drop for the partitioned geometry is less than that for the non-partitioned one due to the corner eddies. The maximum dimensionless temperatures obtained for the partitioned and non-partitioned enclosures are almost the same.

The dimensionless inlet velocity in pure natural convection varies as $Gr^{1/3}$ for the range $10^{10} \leqslant Gr \leqslant 10^{15}$. Computations of pure natural convection in this range with turbulence models are found to revert to laminar regime. The mixed convection results revealed that above a Reynolds number of 5×10^5, the natural convection becomes insignificant. Correlations are constructed for estimating various dimensionless quantities of interest.

References

[1] M.T. Bhoite, G.S.V.L. Narasimham, M.V. Krishna Murthy, Mixed convection in a shallow enclosure with a series of heat generating components, Int. J. Therm. Sci. 44 (2005) 121–135.

[2] P.F. Linden, The fluid mechanics of natural ventilation, Ann. Rev. Fluid Mech. 31 (1999) 201–238.

[3] P.V. Nielsen, A. Restivo, J.H. Whitelaw, Buoyancy affected flows in ventilated rooms, Numer. Heat Tr. 2 (1979) 115–127.

[4] P.V. Nielsen, Some aspects of the air distribution in ventilated rooms, Int. J. Refrig. 5 (1982) 79–85.

[5] J.L. Lage, A. Bejan, Efficiency of transient contamination removal for a slot ventilated enclosure, Int. J. Heat Mass Trans. 34 (1991) 2603–2615.

[6] J.L. Lage, A. Bejan, R. Anderson, Removal of contaminant generated by a discrete source in a slot ventilated enclosure, Int. J. Heat Mass Trans. 5 (1992) 1169–1180.

[7] S. Murakami, S. Kato, Y. Suyama, Three-dimensional numerical simulation of turbulent airflow in a ventilated room by means of a two-equation model, Paper No. 3091, ASHRAE Trans. 93 (2) (1987) 621–642.

[8] T. Kurabuchi, T. Kusuda, Numerical prediction for indoor air movement, ASHRAE J. 29 (12) (1987) 26–30.

[9] H. Wang, S. Touber, Distributed dynamic modelling of a refrigerated room, Int. J. Refrig. 13 (1990) 214–222.

[10] R.J.H. van Gerwen, H. van Oort, The use of fluid dynamics simulation models in cold store design, in: Refrigeration Science and Technology: The Impact of Electro-technology on Refrigeration/Heat Pump Industries, IIR/IIF Commission B2, Bristol (United Kingdom), 1989-1, pp. 233–239.

[11] R.J.H. van Gerwen, H. van Oort, Optimization of cold store design using fluid dynamics models, in: Refrigeration Science and Technology: Progress in the Science of Food Technology and Refrigeration in Food Engineering, IIR/IIF Commissions B2, C2, D1, D2/3, Dresden (Germany), 1990-4, pp. 473–478.

[12] M.L. Hoang, P. Verboven, J. De Baerdemaeker, B.M. Nicolaï, Analysis of the air flow in a cold store by means of computational fluid dynamics, Int. J. Refrig. 23 (2000) 127–140.

[13] E. Papanicolaou, Y. Jaluria, Computations of turbulent flow in mixed convection with a localized heat source, J. Heat Trans. – Trans. ASME 116 (1995) 649–658.

[14] R.A.W.M. Henkes, Natural-convection boundary layers, PhD thesis, Delft University of Technology, Delft, Netherlands, 1990.

[15] R.A.W.M. Henkes, F.F. van der Vlugt, C.J. Hoogendoorn, Natural-convection flow in a square cavity calculated with low-Reynolds-number turbulence models, Int. J. Heat Mass Trans. 34 (2) (1991) 377–388.

[16] B.E. Launder, D.B. Spalding, The numerical computations of turbulent flows, Comput. Method Appl. M. 3 (1974) 269–289.

[17] W.P. Jones, B.E. Launder, The prediction of laminarization with a two-equation model of turbulence, Int. J. Heat Mass Trans. 15 (1972) 301–314.

[18] E. Papanicolaou, V. Belessiotis, Transient natural convection in a cylindrical enclosure at high Rayleigh numbers, Int. J. Heat Mass Trans. 45 (2002) 1425–1444.

[19] B.E. Launder, B.I. Sharma, Application of the energy dissipation model of turbulence to the calculation of flow near a spinning disc, Lett. Heat Mass Trans. 1 (1974) 131–138.

[20] B.E. Launder, B.I. Sharma, Prediction of local heat transfer on a rotating disk by a two-equation model of turbulence, J. Heat Trans. – Trans. ASME 1 (1977) 151–152.

[21] K. Hanjalic, S. Vasic, Numerical simulation of free convection in single- and multiple-zone rectangular cavities, in: G. Hetsroni (Ed.), Heat Transfer 1990: Proc. of the Ninth International Heat Transfer Conference, Jerusalem (Israel), vol. 2, 1990, pp. 579–584.

[22] N.Z. Ince, B.E. Launder, On computations of buoyancy-driven flows in rectangular enclosures, Int. J. Heat Fluid Fl. 10 (1989) 110–117.

[23] A.A. Amsden, F.H. Harlow, A simplified MAC technique for incompressible fluid flow calculations, J. Comput. Phys. 6 (1970) 322–325.

[24] S.V. Patankar, Numerical Heat Transfer and Fluid Flow, Hemisphere Publishing Corporation/McGraw-Hill Book Company, Washington, DC/New York, 1980.

[25] M.-P. Fraikin, J.J. Portier, C.J. Fraikin, Application of a k–ϵ turbulence model to an enclosed buoyancy driven recirculating flow, Chem. Eng. Commun. 13 (1982) 289–314.

[26] N.C. Markatos, K.A. Pericleous, Laminar and turbulent natural convection in an enclosed cavity, Int. J. Heat Mass Trans. 27 (1984) 755–772.

[27] G.O. Roberts, Computational meshes for boundary layer problems, in: M. Holt (Ed.), Proc. of the Second Int. Conf. on Numerical Methods in Fluid Dynamics, Springer-Verlag, Berlin, 1971, pp. 171–177.